

Influences of the compressed dry air-based active cooling on external and internal qualities of wire-arc additive manufactured thin-walled SS308L components

Van Thao Le^{a,*}, Dinh Si Mai^a, Henri Paris^b

^a Le Quy Don Technical University, 236 Hoang Quoc Viet, Bac Tu Liem, Hanoi, Viet Nam

^b Univ. Grenoble Alpes, CNRS, Grenoble INP, G-SCOP, F-3800, Grenoble, France

ARTICLE INFO

Keywords:

Wire-arc additive manufacturing
Active cooling
SS308L
Microstructure evolution
Mechanical properties

ABSTRACT

Among additive manufacturing (AM) technologies, wire-arc additive manufacturing (WAAM) features a high material deposition rate and low costs of device investment. However, WAAM parts generally undergo a complex-thermal history and a high accumulation of heat, which significantly influences its external and internal qualities. In this article, the influence of different cooling conditions on the qualities of WAAM SS308L components was addressed. Three thin walls were built by WAAM with three cooling conditions. The first and second walls were produced with the free-cooling condition, where an interlayer holding time (T_{ih}) of 30 s and 60 s was used between two successive deposits, respectively. The third wall was built with the compressed dry air (CDAir)-based active cooling, in which the compressed dry air (CDAir) and an interlayer holding time of 10 s were employed between two adjacent layers to cool down the workpiece. The obtained results indicate that the evolution of microstructures in three walls is very likable. In the bottom and the middle regions, the microstructure mainly contains vertically oriented dendrites of austenite and ferrites that appear in the austenite grains' boundary. The austenitic phases also appear in equiaxed grains in the top region. However, the CDAir-based active cooling has noticeable effects on the spacing of secondary dendrite arms (SSDA) in the middle of the walls. The wall built with the CDAir-based active cooling features the smallest average SSDA, followed by the walls produced in the free cooling condition and a T_{ih} of 60 s and 30 s, respectively. Accordingly, the CDAir-based active cooling produces the highest average hardness and tensile strengths. Moreover, the wall produced using the CDAir-based cooling also reveals the lowest surface roughness. Therefore, it can be considered that the CDAir-based active cooling is a reasonable option to enhance the internal and external qualities of WAAM stainless steel 308L components.

Introduction

Wire-arc additive manufacturing (WAAM) is a type of metal additive manufacturing (AM) technology. In WAAM, the arc is employed to melt the metal wire, and melted metal is deposited layer-by-layer along the designed paths from a substrate [1]. In comparison to other metal-based AM technologies, WAAM features a high rate of material deposition. The deposition rate of WAAM can reach up to 8 kg/h, while those of directed energy deposition (DED) and powder bead fusion (PBF) are about 2.27 kg/h and 0.1–0.2 kg/h, respectively [2]. That is why WAAM is gaining an increasing interest for the manufacture of large-dimensional parts in different industrial sectors. WAAM also exhibits high energy efficiency

[3] and lower costs of equipment investment [4]. A WAAM system can be easily constructed by integrating a welding power source, a welding torch, and a wire feed system with a CNC machine or a robot [1]. Moreover, the use of the metal wire as the feedstock material is more cost-efficient and safer for operators' health and the environment [5]. Lastly, the production cost of the metallic wire is significantly lower than that of metallic powder [6]. However, WAAM components generally reveal poor surface quality, low-dimensional accuracy, and high distortion and residual stresses [2,6,7].

Similar to other metal-based AM technologies, the qualities of WAAM components strongly depend on processing conditions. Enormous studies have paid attention to investigating the influence of

* Corresponding author.

E-mail address: thaomta@gmail.com (V.T. Le).

<https://doi.org/10.1016/j.jmapro.2020.11.046>

Received 29 August 2020; Received in revised form 25 November 2020; Accepted 30 November 2020

Available online 22 December 2020

1526-6125/© 2020 The Society of Manufacturing Engineers. Published by Elsevier Ltd. All rights reserved.

processing parameters on the shape, microstructures, and mechanical properties of WAAM components. For example, Xiong et al. [8] explored the effects of interlayer temperature, wire-feed speed, and traveling speed on the surface appearance of WAAM H08Mn2Si walls. These authors highlighted that the surface roughness increased with an increase in the interlayer temperature. The augmentation in the wire feed speed also caused a decrease in the surface quality. Dinovitzer et al. [9] stated that the welding current and the traveling speed were two factors which have dominant influences on the geometry of welding beads and the microstructure of WAAM nickel alloys. Gomez Ortega et al. [10] reported the effects of processing parameters on the external quality of CMT (Cold Metal Transfer)-based WAAM Al5Si alloys. In particular, these authors focused on the effects of welding power and traveling speed on the geometry of single deposits and thin walls. Su et al. [11] investigated the effects of heat input on the microstructural evolution and material properties of WAAM aluminum-magnesium alloy parts. They found that the grains could be modified by adjusting the heat input via the control of traveling speed and wire-feed speed. The tensile strengths of components could be enhanced by increasing the traveling speed. Rodrigues et al. [12] paid their attention to the impact of thermal cycles on the quality of WAAM HSLA steel parts. The authors stated that the components built with higher heat input featured lower surface waviness. Nevertheless, the variation of heat input had no noticeable effects on the microstructural and mechanical properties.

As compared to electron beam/laser AM processes, the arc used in WAAM as the energy source generates significantly higher heat input, leading to a high heat accumulation in WAAM components [13,14]. Such an accumulation directly impacts the surface quality, the microstructure evolution, and material properties of parts, because the heat accumulation relates to the cooling rate, the interlayer temperature, and the molten pool size. To overcome this problem, most of the previous studies used the interlayer idle/dwell/holding time between successive deposited layers to reduce the heat accumulation and interlayer temperature [15–17]. The interlayer holding time enables the part to cool down to a certain value of interlayer temperature before the deposition of the next layer. However, to keep the interlayer temperature at a constant value, the interlayer holding time must be more and more increased at higher layers [16], leading to a productivity loss.

In order to reduce the interlayer holding time and heat accumulation, a number of studies have used active cooling systems. There are generally two types of active cooling systems, in which either compressed air/gas or water was used for the cooling. Wu et al. [18,19] employed a compressed CO₂ gas directly sprayed on the upper surface of deposits in the case of WAAM thin-walled titanium alloy components. These authors emphasized that this active cooling approach with CO₂ allows the heat accumulation and the thermal distortion of parts to be mitigated. This cooling method could also enhance microhardness and tensile properties of titanium alloy components produced by WAAM. For materials less reactive to the ambience, the compressed-dry air (CDAir) was normally employed. For example, Montevecchi et al. [20] and Hackenhaar et al. [21] employed the CDAir for the cooling purpose and evaluated its influence on the accumulation of heat in the build of thin-walled ER70S-6 parts by WAAM. These authors found that this CDAir cooling method limited the increase of the interlayer temperature. The main advantages of using the CDAir in active cooling systems are low costs and its availability in workshops. Concerning the active cooling with water, Nagamatsu et al. [22] designed a chamber of water, in which the level of water was manually adjusted to cool down manufactured components during the production process. Silva et al. [23] also integrated a water-based cooling system in the WAAM process, and the built wall was dipped in a water tank. The performance of this approach was validated via the building of Al5Mg thin walls. These authors proved that by using such a cooling system, both the external and internal qualities of fabricated components were improved when compared to the free cooling approach. However, the water-based cooling systems generally restricted the flexibility of WAAM systems

[24]. Briefly, it is found that the CDAir-based active cooling seems more effective and economical.

Until now, most of the published studies focused on exploring the external and internal qualities of WAAM titanium/aluminum/nickel-based alloy components [7,25]. For WAAM of steels, low-carbon steels and some austenite stainless steels (e.g. 304, 304L and 316L) were mostly used as the feedstock material [26,27]. Rafieezad et al. [28] fabricated multi-track multi-layer low-carbon steel components manufactured by WAAM, while Le [29] used such a technique to build single-track multi-layer low-carbon steel components. Haden et al. [30] used a WAAM system to build thin-wall components from ER70S and 304 steels. These authors focused on studying the microstructure and the mechanical characterization of WAAM ER70S/304 steel components. Many authors paid their attention to the fabrication of 316L steels by WAAM [31–34]. They proved that the microstructure of WAAM thin-walled 316L components consists of dominant austenite phases and a small amount of ferrite and sigma phases, which appear in grain boundaries of the austenite matrix. Among austenite stainless steels, 308L stainless steels feature a low level of carbon, high corrosion resistance and high mechanical properties. This alloy is widely employed in oil, gas, and mining industries. However, the manufacture of SS308L components by WAAM is rarely discussed. Few studies employed 308LSi and 308L as the feedstock material in laminar plasma-based AM, and laser-based metal deposition. Abioye et al. [35] used a laser metal wire deposition process to build single-track multi-layer 308LSi components, while Li et al. [36] fabricated a hollow component composed of four straight walls by using laminar plasma AM.

To bridge the aforementioned research gap, we have recently conducted the first studies on the manufacture of SS308L components by WAAM [37,38], in which we focused on the optimization of process parameters, the microstructural and mechanical properties of WAAM SS308L components. In the current research, the CDAir-based active cooling was taken into consideration for the purpose of enhancing internal and external qualities of WAAM stainless steel 308 L parts and the production rate. The influences of the CDAir-based active cooling on the surface's quality, the microstructural and mechanical characteristics of WAAM SS308L parts were particularly clarified. To prove the performance of such an active cooling method, a comparison with the free cooling method was also performed.

Materials and experimental methods

In the current research, the commercial SS308 L wire with the size of 1 mm in diameter was employed as the feedstock in the WAAM process. The chemical composition of the wire includes 19.5%–21% of Cr, 9%–11% of Ni, 0.5% (max) of Mo, 0.75% (max) of Cu, 0.3%–0.65% of Si, 1%–2.5% of Mn, 0.03% (max) of C/P/S, and the balance of Fe. To study the influence of different cooling conditions on the quality of WAAM parts, three thin walls of 18 layers and a length of 120 mm were deposited on low carbon steel (SS400) plates by a welding robot (Panasonic TA-1400, as shown in Fig. 1a).

The power supply used to generate the electric arc between the consumable electrode and the workpiece is Panasonic YD-350GR3. For this WAAM system, the wire feed speed is automatically adjusted according to the welding current. The wire feed speed generally increases with an increase in the welding current, as depicted in [8]. The substrate size is 250 mm x 150 mm x 10 mm in length, width, and thickness, respectively.

All three walls were built according to the same depositing direction strategy (Fig. 1b) and employing the similar process parameters: a voltage of 20 V, a travel speed of 368 mm/min, and a current of 122 A [37]. The distance between the welding torch and the substrate or the deposited layer is 12 mm. During the depositing process, a gas of 99.9% argon was employed for the shielding purpose. The flow rate of the shielding gas was fixed at 15 L/min. The first wall and the second wall

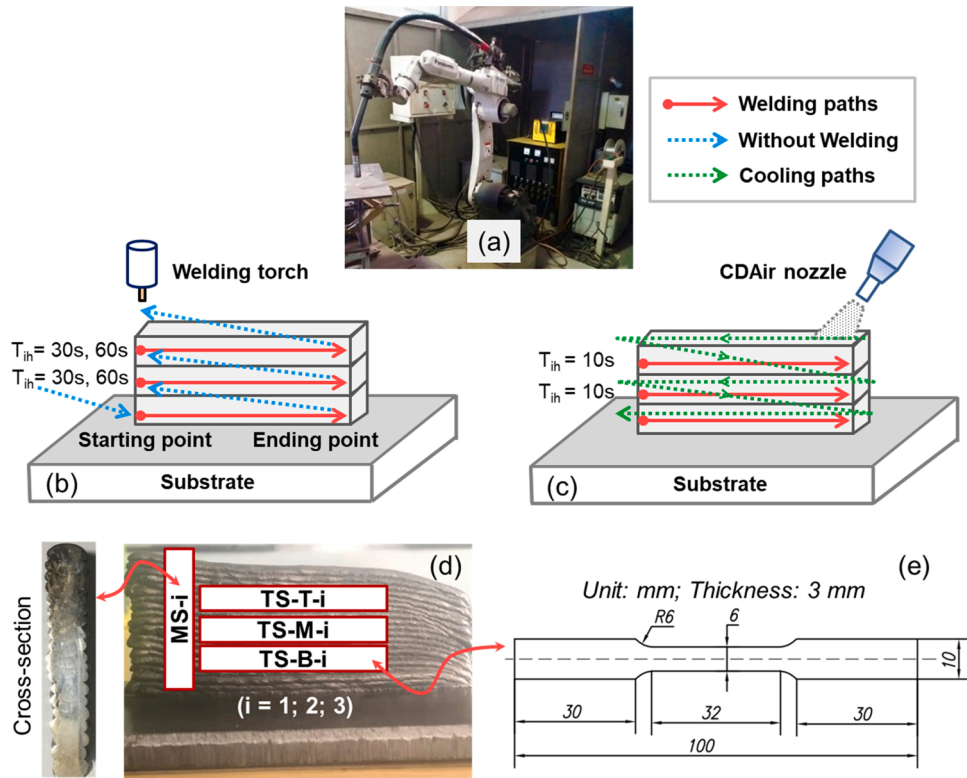


Fig. 1. WAAM system (a), the depositing strategy for the build of the first wall, the second wall with the free cooling (b), and of the third wall with the active cooling (c), the built wall with the positions for cutting the specimens to investigate the microstructures and hardness (MS-i) and three tensile samples (TS-T-i, TS-M-i, and TS-B-i), with $i = 1; 2; 3$ for the first, the second and the third wall (d), and the dimensions of tensile samples (e).

were manufactured with the free-cooling method, where an interlayer holding time (T_{ih}) of 30 s and 60 s, respectively, was used between two adjacent deposits for cooling down the walls (Fig. 1b). Whereas, during the building of the third wall, an interlayer holding time of 10 s and the CDAir-based active cooling were applied to cool down the wall rapidly between two adjacent deposits (Fig. 1c). In this case, once a deposit was finished, the compressed dry air (CDAir) was manually sprayed on the top surface and on a side surface of the wall from the top to the bottom of the wall by using a commercially-available air pressure nozzle, as illustrated in Fig. 1c. The flow rate of the CDAir is 240 L/min. The operating pressure of the air is 0.6 MPa, and the temperature of the

CDAir at the nozzle tip is 16 °C.

Once the walls were built completely, they were cleaned and the oxidized film on both side surfaces of the walls was removed by a stainless steel wire brush. Subsequently, the sizes and shape of the walls were obtained by using a non-contact three-dimensional digitizer (Konica Minolta Range 7). The surface roughness of the side surfaces was estimated using the method proposed in [8]. From the point cloud $\{P_i(X_i, Y_i, Z_i)_{i=1 \text{ to } N_p}\}$ in the effective area of the side surfaces (Fig. 2), a least square fitting plane (Q): $\alpha X + \beta Y + \gamma Z + \delta = 0$, where $\alpha^2 + \beta^2 + \gamma^2 \neq 0$, was firstly estimated. Then the surface roughness (SR) of the side surfaces was computed by Eq. (1), where D_i is the distance from the point

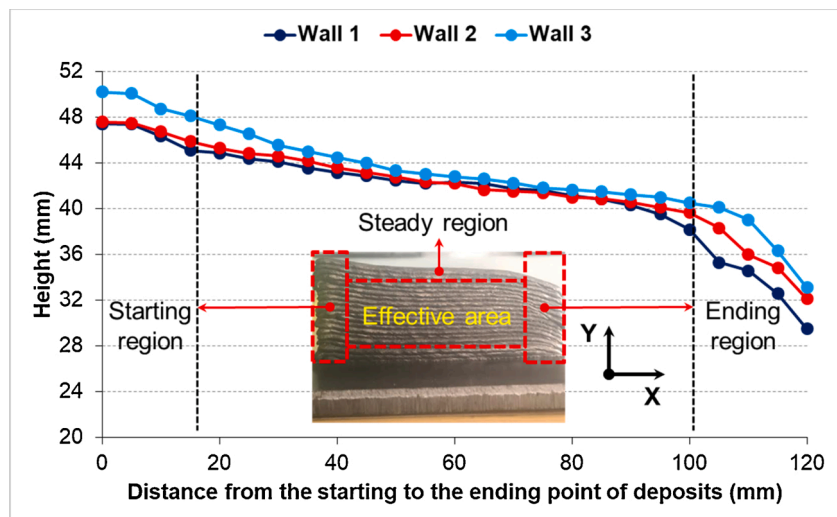


Fig. 2. The height variation of the walls.

P_i to the plane (Q):

$$SR = \frac{1}{N_p} \left(\sum_{i=1}^{N_p} D_{i(P_i \rightarrow (Q))} \right) = \frac{1}{N_p} \left(\sum_{i=1}^{N_p} \frac{|\alpha X_i + \beta Y_i + \gamma Z_i + \delta|}{\sqrt{\alpha^2 + \beta^2 + \gamma^2}} \right) \quad (1)$$

In each wall, to analyze the microstructure and material properties, a sample (MS-i) was employed to investigate the microstructures and hardness, and three tensile samples (TS-T-i, TS-M-i, and TS-B-i) in the horizontal direction had been prepared (Fig. 1d). Here, i was equal to 1, 2, and 3 for the first, the second, and the third walls, respectively. The dimensions of all tensile specimens were selected based on the ASTM E8M-13 standard (Fig. 1e).

A Vickers microhardness tester Duramin-2 of Struers and a microscope AXIO imager A2M of Carl Zeiss were employed to analyze the hardness and the microstructure of the walls, respectively. For each microhardness test, a load of 980.7 mN and a dwell time of 10 s were applied. The tensile strength tests were implemented on a tensile testing machine (INSTRON 3 T, Model 5967B12620). The tensile experiment was performed at ambient temperature. The speed of the crosshead is 0.01 m/min. The fracture surface morphologies of the tensile specimens were observed by using a scanning electron microscope (SEM) (SU3500).

The chemical composition of the WAAM SS308L walls was also analyzed by using a Thermo Scientific Spectrometer (ARL3460 OES). It is observed that the percentage of chemical elements of WAAM SS308L walls falls within the same value range as that of the commercial SS308L wire, as shown in Table 1.

Results and discussion

Quality of WAAM thin-walled components

Fig. 2 shows the typical shape of WAAM SS308L walls built with the same depositing direction strategy. The height of the walls generally decreases from the starting point to the ending point of deposited layers. It was also found that the first and the second walls reveal a nearly identical height except in the ending region. On the other hand, the third wall exhibits a relatively higher height in comparison to the first and the second walls. Moreover, the third wall shows the smallest surface roughness ($SR = 0.17$ mm), whereas the first wall features the highest value ($SR = 0.24$ mm), and that of the second wall is 0.22 mm (Fig. 3). It is noted that these SR values were computed in the effective area of the side surfaces (Fig. 2).

According to the findings reported in [17,39], an increase in the interlayer holding time within a certain range leads to an improvement of the surface quality. In this study, the first and the second walls were produced with the free-cooling method, and T_{ih} is equal to 30 s and 60 s, respectively. Therefore, the surface roughness of the second thin wall is relatively lower than that of the first thin wall (0.22 mm vs. 0.24 mm). Moreover, the interlayer holding time is also contributed to the interlayer temperature, the cooling rate, and the temperature gradient of deposited parts [21,39].

In the cases of the first and the second walls, the temperature of the deposited layer was gradually reduced to a certain value by the ambient air, whereas, in the building of the third wall, the temperature of the current layer and the whole wall were reduced rapidly by the compressed dry air [21]. Hence, the accumulation of heat and the cooling time of the third thin-walled part must be significantly lower than those in the first and the second walls. With a high heat accumulation and a

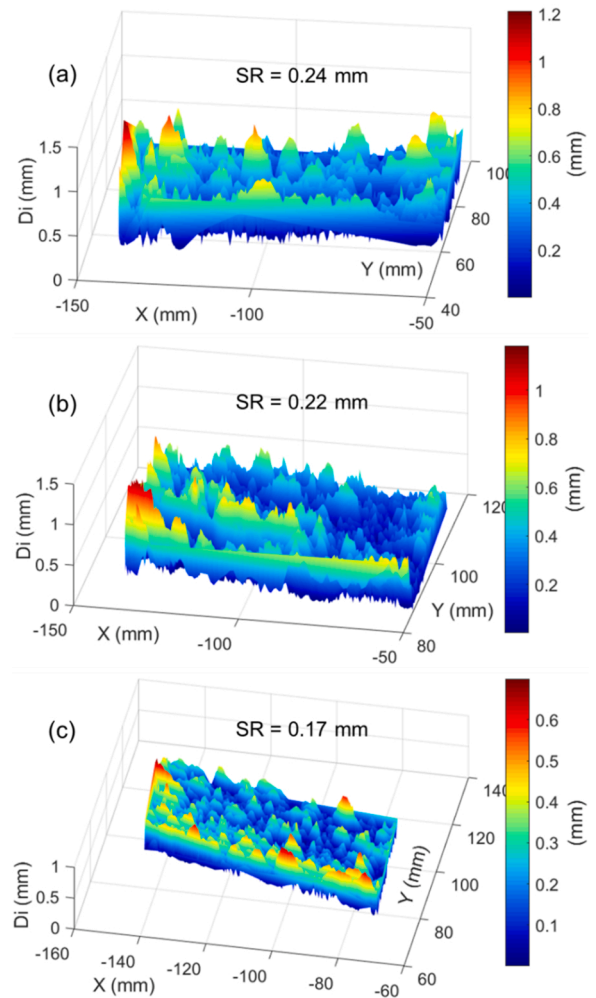


Fig. 3. Surface roughness of the walls: (a), (b), and (c) corresponding to the first, the second, and the third wall, respectively.

high interlayer temperature, the molten pool was overflowed, leading to a thinner layer thickness, and a higher surface roughness [8]. As a result, the surface roughness of the third wall is lower than those of the first and the second walls (0.17 mm vs. 0.24 mm and 0.22 mm), whereas the layer thickness of the third wall is higher than those of the first and the second walls. Accordingly, the total height of the third wall is the highest, as observed in Fig. 2.

In order to observe the internal quality of parts, all microstructure specimens (MS-i) and all tensile specimens were tested through the X-ray CT tests. Fig. 4 reveals the cross-section morphology of the walls, which was extracted from X-ray CT scanned data on the specimens (MS-i), and Fig. 5 shows representative X-ray CT images of tensile specimens of the walls. In X-ray CT images, the background and defects are generally displayed in black, whereas the parts appear in white. It is found that no black zones were observed in the (MS-i) and tensile specimens. This indicates that all thin walls were successfully produced by the WAAM process without major defects, for example, macroporosity, cracks, and improper fusion between successive deposits in both the building direction and the transversal direction. In comparison

Table 1

Chemical composition of the WAAM thin-walled SS308L component and the SS308L wire.

Element	C	P	S	Cr	Ni	Mo	Cu	Si	Mn	Fe
The WAAM SS308L wall	0.009	0.029	0.016	20.02	10.12	0.029	0.103	0.56	1.66	Bal.
The SS308L wire	0.03 max	0.03 max	0.03 max	19.5 - 21	9.0 - 11.0	0.50 max	0.75 max	0.30 - 0.65	1.0 - 2.5	Bal.

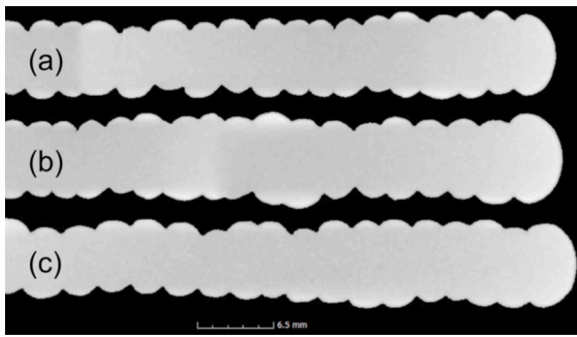


Fig. 4. (a), (b), and (c) X-ray CT images of a cross-section of the first, the second, and the third wall, respectively.

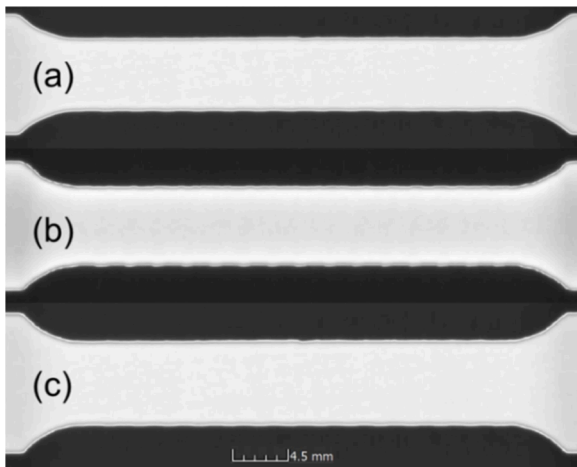


Fig. 5. (a), (b), and (c) X-ray CT images of the tensile specimens (TS-M-1), (TS-M-2), and (TS-M-3), respectively.

to other metal-based AM technologies, for example, selective laser melting (SLM), electron beam melting (EBM), and laser metal deposition (LMD) [40], manufactured parts generally feature pores because the metal powder was not completely melted, and so on [41]. This phenomenon has significant impacts on mechanical properties of parts, especially dynamic properties such as fatigue strength [42,43].

Microstructures

It is firstly observed that all thin walls feature the same microstructure evolution. Fig. 6 shows the microstructure of the first wall, which is representative for the microstructure of SS308L steel walls produced by WAAM. The microstructure of WAAM SS308L walls mainly consists of austenitic phases (in white) and remaining ferrites (in black), which remain in the austenite matrix boundary. The austenitic phases are mostly exhibited in the form of columnar structures (Fig. 6b, c and b-1) and a small amount of granular/equiaxed grains in the top of deposited layers as well as in the top region of the walls (Fig. 6a and b-2), whereas the ferrite phases appear in skeletal and lathy morphologies. Indeed, the mode of solidification of WAAM thin-walled SS308L components depends on the ratio between the percentages of chromium and nickel equivalents, which were determined by the formula of Schaeffler [44], as shown in Eq. (2) and Eq. (3), respectively:

$$\%Cr_{eq} = \%Cr + 0.5 \cdot (\%Nb) + 1.5 \cdot (\%Si) + \%Mo \quad (2)$$

$$\%Ni_{eq} = \%Ni + 0.5 \cdot (\%Mn) + 30 \cdot (\%C) \quad (3)$$

From the analyzed data in Table 1, $\%Cr_{eq}$, $\%Ni_{eq}$, and Cr_{eq}/Ni_{eq} equal 20.889 %, 11.22 %, and 1.86, respectively. As $1.48 \leq Cr_{eq}/Ni_{eq} =$

$1.86 \leq 1.95$, the structure of WAAM SS308 L walls was formed and developed as follows [44–46]:

$$L \rightarrow (L + \delta) \rightarrow (L + \delta + \gamma) \rightarrow (\gamma + \delta) \quad (4)$$

As described in Eq. (4), the primary ferrite phases (δ) were firstly generated from the liquid phase (L). After that, the austenite phases (γ) were secreted and developed during the rapid cooling and solidification processes. Finally, the austenite dendrites replaced the primary ferrite phases. The residual ferrite rests in the form of skeletal and lathy structures in the grain boundaries of austenite dendrites.

Moreover, the microstructure of WAAM 308L thin walls can be distinguished in three regions: the top (i.e. the latest deposited layer, Fig. 6a), the middle (Fig. 6b), and the bottom of the walls (Fig. 6c). This is because the temperature history, the cooling rate and the solidification time are different in these regions. In the bottom region, very thin columnar structures were developed nearly vertically along the building direction (Fig. 6c). There is no visible difference in terms of microstructures in the bottom region between three walls. In fact, the temperature in the first deposited layer was rapidly transferred and dissipated to the substrate assumed to be at room temperature. In this region, the active cooling did not significantly influence the interlayer temperature, the solidification time, and the cooling rate [21,39].

In the top region of the walls, the microstructure is dominantly characterized by granular/equiaxed grains (Fig. 6a). In comparison to the microstructure in other regions, the grains of the top are coarser. Indeed, the latest layer of the walls was not affected by the reheating process as other layers. The top of the molten pool of this layer directly contacts the natural air; thereby it was solidified into steering dendrites, whereas the bottom of the molten pool was solidified into columnar dendrites according to the epitaxial growth. The center of this layer is the final solidification zone. As the temperature gradient is suppressed in the center, the columnar dendrites were transferred into equiaxed grains [45].

Fig. 6 presents the typical microstructure in the middle region of the walls. In this region, the microstructure evolution in different layers can clearly be observed. Within a specified layer, austenite grains develop nearly vertically along the building direction. At the bottom of the layer, cellular structures can be found close to the fusion line. They were subsequently developed into finer columnar structures in the middle of the layer (Fig. 6b-2). The columnar structures gradually grow along the height of the layer, and finally transform into coarser columnar/granular grains at the top of the layer (Fig. 6b-1). The coarse grains at the top of the layer can be considered the results of the reheating and partially remelting processes caused by the heat of the next layer. As a result, far away from the bottom of the layer, it is easy to distinguish secondary dendrites (Fig. 6b).

To clarify the influence of different cooling conditions on the microstructure of WAAM thin-walled SS308L components, the microstructure of the same layer in the middle region of three walls was taken into consideration for comparison. The spacing of secondary-dendrite arms (SSDA) at the top, in the center, and at the bottom of the layer was measured by using the ImageJ software, as shown in Fig. 7. It is found that, in three cases, the average SSDA gradually augments from the bottom of the layer to the top of the layer. For example, in the case of the first wall, the average SSDA at the bottom, in the middle, and at the top of the layer is $8.20 \pm 0.49 \mu\text{m}$, $10.52 \pm 0.33 \mu\text{m}$, $12.64 \pm 0.86 \mu\text{m}$, respectively. Moreover, in the whole layer, the wall fabricated with the CDair-based cooling features the smallest average SSDA, followed by the walls produced with the free-cooling condition and $T_{ih} = 60 \text{ s}$ and $T_{ih} = 30 \text{ s}$. For instance, in the middle of the layer, the average SSDA of the third wall, the second wall, and the first wall is $8.63 \pm 0.38 \mu\text{m}$, $9.62 \pm 0.41 \mu\text{m}$, $10.52 \pm 0.33 \mu\text{m}$, respectively.

This phenomenon is interpreted by the effect of different cooling conditions. Due to the CDair-based active cooling, the interlayer temperature in the third wall is the lowest. The interlayer temperature of the second thin wall is also lower than that of the first thin wall, because the

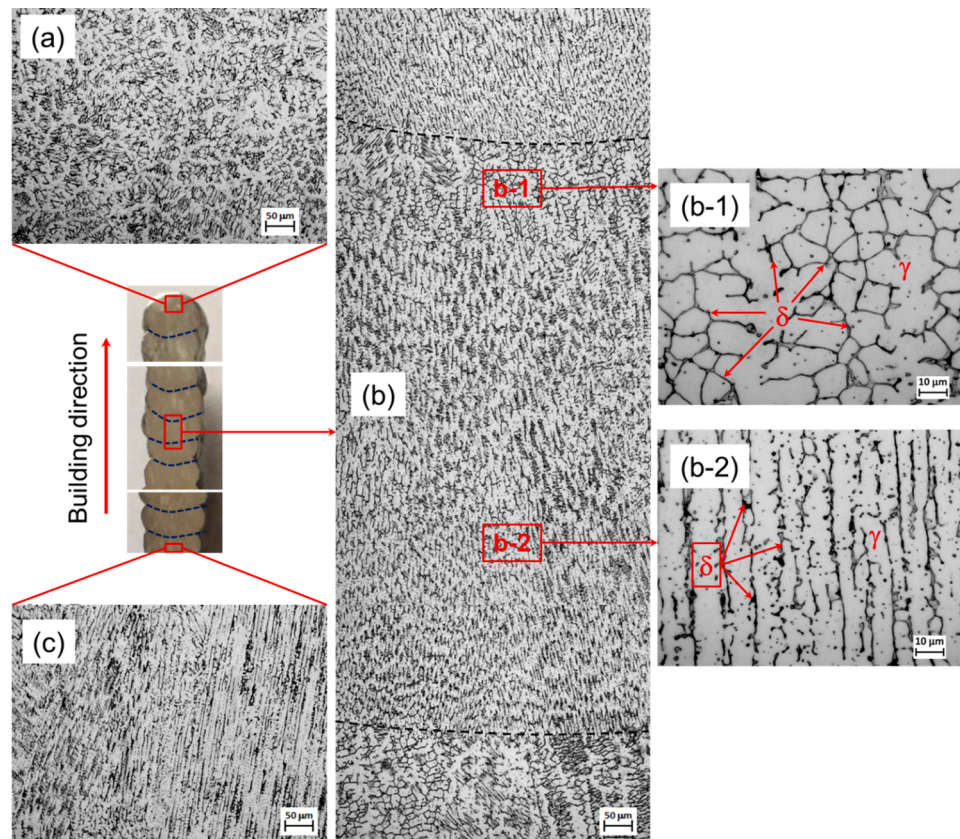


Fig. 6. Microstructures at low magnification (x100) in the top region (a), the central region (b), and the bottom region (c) of the walls, the microstructure at high magnification (x500) at the top (b-1), at the bottom and in the middle (b-2) of a layer.

interlayer holding time in the building of the second wall is longer (60 s vs. 30 s). As the interlayer temperature increases, the cooling and solidification processes become longer, while the cooling rate (CR) decreases [17,39,47]. In addition, the SSDA increases with a decrease in the cooling rate according to the relationship: $SSDA = 50 \cdot (CR)^{-0.4}$, herein CR is measured in K/s [47,48]. Consequently, the cooling rate in the building of the third wall is the highest, leading to the smallest SSDA. As the cooling rate in the building of the first thin wall is slower than that of the second thin wall, the SSDA of the first thin wall is greater than that in the second thin wall. Furthermore, because of the active cooling during the building of the third wall, it is assumed that the interlayer temperature remains constant. Thereby, the average SSDA of all layers in the middle region is relatively equal. On the other hand, in the thin walls fabricated with the free-cooling condition, the heat accumulation increases with the number of deposited layers. As a result, the interlayer temperature at higher layers is relatively higher than that at lower layers. Accordingly, the SSDA in higher deposited layers is relatively larger than that in the lower deposited layers.

Based on the above comparison, it can be concluded that the SSDA induced by the CDAir-based active cooling is smaller than that produced by the free-cooling conditions. In addition, the SSDA between lower layers and higher layers in the central region of the thin wall produced with the CDAir-based cooling is relatively similar. On the other hand, in the free-cooling method, an increase in the interlayer holding time (T_{ih}) leads to a smaller SSDA, and the SSDA in the lower layers is smaller than that in the higher layers of the walls.

Hardness

Fig. 8a shows the average microhardness (HV0.1) in three regions of the walls. In the bottom region and the top region of the walls, the hardness was measured at six points. In the middle region, the hardness

was measured in four successive layers. The hardness measurement was also carried out at six points for each layer. In each region, the measurement points of hardness were distributed on the centerline of the cross section. The hardness variation in the middle region of the walls is revealed in Fig. 8b.

It is observed that, for all three walls, the average hardness reduces from the bottom region to the top region of the walls. For example, for the first wall, the average hardness is equal to 169.17 ± 3.07 (HV0.1), 156.45 ± 3.80 (HV0.1), and 150.45 ± 2.73 (HV0.1) in the bottom region, in the middle, and in the top region, respectively. This is because, for all three walls, the bottom region reveals the thinnest columnar structures, which grow and become larger in the middle region, and finally transform into coarser equiaxed/granular grains in the top region of the walls.

Additionally, there is no substantial deviation in terms of the average hardness between the walls in both the top and the bottom regions (Fig. 8a). In the bottom region, the average hardness is 169.17 ± 3.07 (HV0.1), 168.73 ± 2.94 (HV0.1), and 169.25 ± 3.12 (HV0.1) for the first wall, the second wall, and the third wall, respectively. The average hardness in the top region is 150.45 ± 2.73 (HV0.1), 150.65 ± 2.42 (HV0.1), and 151 ± 2.61 (HV0.1) for the first wall, the second wall, and the third wall, respectively. As aforementioned, in the bottom region (i.e. the first deposited layer), there is no substantial difference in the SSDA between the walls. This is because the heat of the first deposit was rapidly dissipated through the large substrate. As a result, the cooling rate in the bottom region of three walls is nearly equal. The latest deposit was not affected by the reheating process and it was freely cooled down to room temperature. Thus, there is also no significant difference in grain size.

In the middle region, the effect of different cooling conditions was clearly shown (Fig. 8a). As mentioned above, the SSDA produced by the CDAir-based active cooling is smaller than that produced by the free

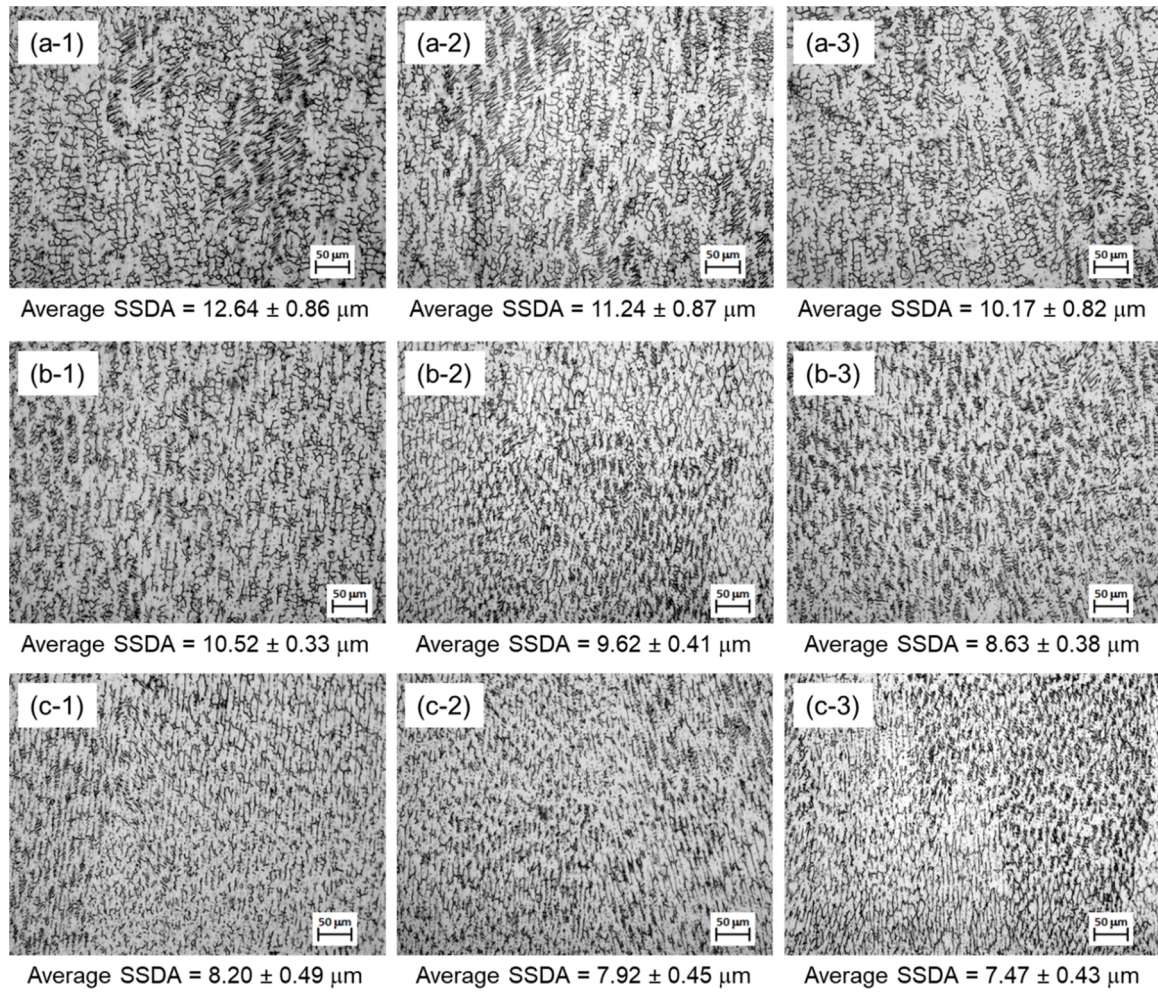


Fig. 7. Microstructures at the top (a-i), in the middle (b-i), and at the bottom (c-i) a layer in the middle region of the wall (i), where $i = 1, 2$ and 3 .

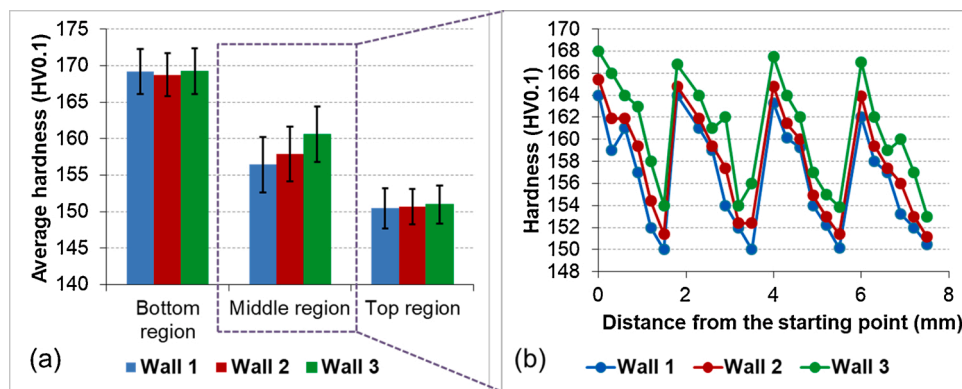


Fig. 8. (a) Average hardness in three regions of the walls and (b) hardness measured on the central line of four adjacent deposits in the central/middle region of the thin walls.

cooling. The SSDA produced by the free cooling with a T_{ih} of 60 s is also smaller than that produced by the free cooling with a T_{ih} of 30 s. Therefore, in accordance with the Hall-Petch relation [49], the third wall reveals the highest average hardness (160.59 ± 3.83 HV0.1), whereas the first wall shows the smallest average hardness (156.45 ± 3.71 HV0.1). The average hardness of the second thin-walled part in the central location is 157.88 ± 3.77 (HV0.1). Moreover, in each layer and for all cases, the microhardness increases from the top to the bottom of the deposited layer (Fig. 8b). This is in good agreement with the

decrease of SSDA from the top to the bottom of the layer. Because of the effect of the CDAir-based active cooling, the average hardness of each layer in the middle region of the third wall is mostly equal. On the other hand, for the free cooling, the average hardness in each layer slightly decreases with an increase in the layer level.

Tensile properties

Fig. 9 reveals three stress-strain curves of three horizontal tensile

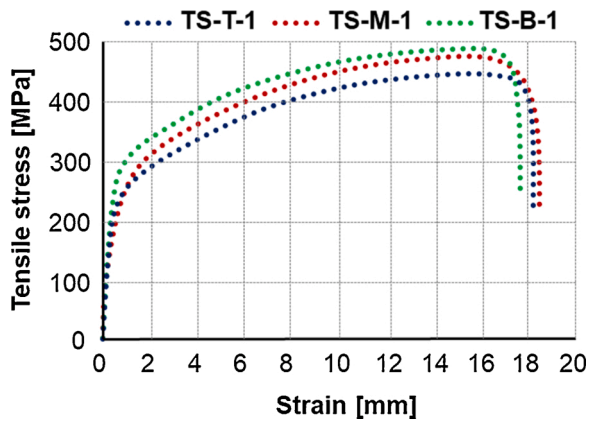


Fig. 9. Stress-strain curves of horizontal tensile specimens extracted from the first wall.

specimens extracted from the first wall, which are representative for all horizontal tensile specimens of WAAM SS308L thin walls. The specimens TS-T-i and TS-B-i are close to the top and the bottom region of the walls, and the specimen TS-M-i is in the middle of the wall. In general, the stress-strain curve of WAAM SS308L contains a region of elastic deformation at the beginning of the load application and followed by a region of plastic deformation before the breaking.

Table 2 summarizes the results of all tensile tests. It is found that the third wall built with the CDAir-based active cooling exhibits the highest average value of yield strength (YS), ultimate tensile strength (UTS), and elongation ($YS = 305.67 \pm 2.08$ MPa, $UTS = 494.67 \pm 10.26$ MPa, and elongation = 55.33 ± 0.58 %), followed by the second wall ($YS = 275.67 \pm 15.53$ MPa, $UTS = 472.33 \pm 11.06$ MPa, and elongation = 54 ± 1 %) and the first wall ($YS = 263.67 \pm 33.65$ MPa, $UTS = 467.67 \pm 9.29$ MPa, and elongation = 50.67 ± 1.15 %).

Moreover, in all three walls, the tensile strengths (YS and UTS) increase from the top to the bottom of the walls. The tensile specimen (TS-B-i) close to the bottom region features the highest average values of YS and UTS. The specimens (TS-B-i) close to the top region show the smallest YS and UTS values. The main reason is related to the SSDA produced by different cooling conditions, as mentioned in Section 3.2. Based on the Hall-Petch relationship [49], as a smaller SSDA was generated, better tensile strengths were achieved.

In the central region, the third wall produced with the CDAir-based cooling features the smallest SSDA, followed by the second wall and the first wall, which were produced with the free-cooling method and $T_{ih} = 60$ s and $T_{ih} = 30$ s, respectively. Therefore, the third wall reveals the

Table 2
The results of tensile tests.

Specimen	YS (MPa)	UTS (MPa)	Elongation (%)
TS-T-1	239	460	50
TS-M-1	250	465	52
TS-B-1	302	478	50
Average	263.67 ± 33.65	467.67 ± 9.29	50.67 ± 1.15
TS-T-2	263	462	54
TS-M-2	271	471	53
TS-B-2	293	484	55
Average	275.67 ± 15.53	472.33 ± 11.06	54 ± 1
TS-T-3	305	486	56
TS-M-3	304	492	55
TS-B-3	308	506	55
Average	305.67 ± 2.08	494.67 ± 10.26	55.33 ± 0.58
Annealed/rolled SS308L [36]	205	515	40

highest average values of tensile strengths, while the first wall shows the smallest average values.

Another observation is that, in the cases of the thin walls produced with the free-cooling method (i.e., the first wall and the second wall), the deviation in terms of YS between the tensile specimens is great. The standard deviation of YS (SD_{YS}) for the first wall and the second wall is 33.65 MPa and 15.53 MPa, respectively, whereas that of the wall produced with the CDAir-based cooling is significantly smaller ($SD_{YS} = 2.08$ MPa). This indicates that the wall produced with the CDAir-based cooling exhibits the YS more homogenous than the walls produced with the free-cooling method. This observation also agrees with the microstructure produced by the CDAir-based active cooling, because there is no significant difference in the SSDA between the layers in the central region of the third thin wall.

Lastly, the tensile strengths and elongation of WAAM thin-walled SS308 L components obtained in this study are also comparable to those reported in the study of Li et al. [36], in which the SS308L was manufactured by laminar plasma-based direct energy deposition. In comparison to annealed/rolled 308L stainless steels, the UTS of WAAM SS308L walls are smaller, whereas the YS and elongation are higher (Table 2).

Fig. 10 presents the morphologies of fractured surfaces of three tensile specimens (TS-M-i, $i = 1; 2; \text{ and } 3$), which are representative for all tensile specimens of three walls. Enormous equiaxed dimples were visibly observed on the fractured surfaces. This indicates the ductile fracturing mode of WAAM SS308L steels, and the as-built material has a good toughness [34,50]. It is also found that the dimples of the wall produced with the CDAir-based cooling (Fig. 10c) are relatively deeper and larger than those of the first wall (Fig. 10a) and the second wall (Fig. 10b). This explains why the third wall features higher plasticity, as shown in Table 2.

Conclusions

In this research, the influence of different cooling conditions of the internal and external qualities of WAAM stainless steel 308L thin walls was investigated. The main findings of this study are epitomized as follows:

- The increase in the interlayer holding time in the free cooling also improves the surface quality of WAAM SS308L walls. However, the more interlayer holding time was used, the less productivity was obtained. By using the CDAir-based active cooling, the surface quality of WAAM SS308L walls can be significantly enhanced. The surface roughness of the walls produced by the CDAir-based active cooling can be reduced by 29 % when compared with the walls built with the free cooling and a $T_{ih} = 30$ s.
- The WAAM SS308L thin walls built with different cooling conditions reveal similar microstructure characterization. The microstructure of WAAM SS308L walls consists of dominant austenite phases and residual ferrite, which remain in the boundaries of austenite grains. In the middle region of the walls, the microstructure of each layer generally exhibits finer columnar structures at the bottom of the layer. They gradually develop and are found to be larger in the middle of the layer, and finally transform into coarser granular/equiaxed grains at the top of the layer.
- The walls built with the CDAir-based active cooling feature the spacing of secondary dendrite arms (SSDA), which is smaller than that of the walls produced by the free cooling method. As a result, the tensile strengths of the walls built with the CDAir-based active cooling are noticeably higher than those of the walls built with the free cooling method.
- Based on the obtained results, it can be considered that the CDAir-based active cooling is a good solution to enhance the external and internal qualities of WAAM SS308L components, as well as productivity.

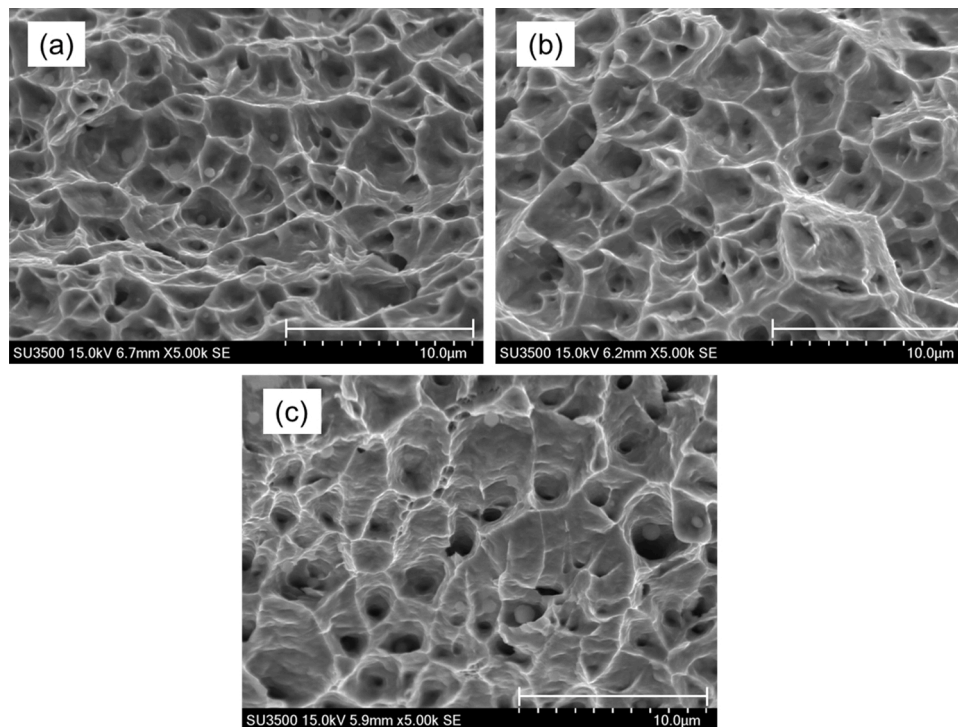


Fig. 10. SEM images of fractured surface morphology of tensile specimens TS-M-1 (a), TS-M-2 (b), and TS-M-3 (c) of the walls (1), (2), and (3), respectively.

Declaration of Competing Interest

The authors declare that they have no known competing financial interests or personal relationships that could have appeared to influence the work reported in this paper.

Acknowledgements

This research is funded by the Vietnam National Foundation for Science and Technology Development (NAFOSTED), under the grant number 107.99-2019.18. The authors sincerely thank Dr. Viet-Khoa Tran-Nguyen for his careful English editing. He is currently a lecturer-researcher at the Faculty of Pharmacy, University of Strasbourg, France.

References

- [1] Cunningham CR, Flynn JM, Shokrani A, Dhokia V, Newman ST. Invited review article: strategies and processes for high quality wire arc additive manufacturing. *Addit Manuf* 2018;22:672–86. <https://doi.org/10.1016/j.addma.2018.06.020>.
- [2] Williams SW, Martina F, Addison AC, Ding J, Pardal G, Colegrove P. Wire + arc additive manufacturing. *Mater Sci Technol* 2016;32:641–7. <https://doi.org/10.1179/1743284715Y.0000000073>.
- [3] Lu X, Zhou YF, Xing XL, Shao LY, Yang QX, Gao SY. Open-source wire and arc additive manufacturing system: formability, microstructures, and mechanical properties. *Int J Adv Manuf Technol* 2017;93:2145–54. <https://doi.org/10.1007/s00170-017-0636-z>.
- [4] Karunakaran KP, Suryakumar S, Pushpa V, Akula S. Low cost integration of additive and subtractive processes for hybrid layered manufacturing. *Robot Comput Integr Manuf* 2010;26:490–9. <https://doi.org/10.1016/j.rcim.2010.03.008>.
- [5] Chang YJ, Sproesser G, Neugebauer S, Wolf K, Scheumann R, Pittner A, et al. Environmental and social life cycle assessment of welding technologies. *Procedia Cirp* 2015;26:293–8. <https://doi.org/10.1016/j.procir.2014.07.084>.
- [6] Ding D, Pan Z, Cuiuri D, Li H. Wire-feed additive manufacturing of metal components: technologies, developments and future interests. *Int J Adv Manuf Technol* 2015;81:465–81. <https://doi.org/10.1007/s00170-015-7077-3>.
- [7] Wu B, Pan Z, Ding D, Cuiuri D, Li H, Xu J, et al. A review of the wire arc additive manufacturing of metals: properties, defects and quality improvement. *J Manuf Process* 2018;35:127–39. <https://doi.org/10.1016/j.jmapro.2018.08.001>.
- [8] Xiong J, Li Y, Li R, Yin Z. Influences of process parameters on surface roughness of multi-layer single-pass thin-walled parts in GMAW-based additive manufacturing. *J Mater Process Technol* 2018;252:128–36. <https://doi.org/10.1016/j.jmatprotec.2017.09.020>.
- [9] Dinovitzer M, Chen X, Laliberte J, Huang X, Frei H. Effect of wire and arc additive manufacturing (WAAM) process parameters on bead geometry and microstructure. *Addit Manuf* 2019;26:138–46. <https://doi.org/10.1016/j.addma.2018.12.013>.
- [10] Gomez Ortega A, Corona Galvan L, Deschaux-Beaume F, Mezrag B, Rouquette S. Effect of process parameters on the quality of aluminium alloy Al5Si deposits in wire and arc additive manufacturing using a cold metal transfer process. *Sci Technol Weld Join* 2018;23:316–32. <https://doi.org/10.1080/13621718.2017.1388995>.
- [11] Su C, Chen X, Gao C, Wang Y. Effect of heat input on microstructure and mechanical properties of Al-Mg alloys fabricated by WAAM. *Appl Surf Sci* 2019;486:431–40. <https://doi.org/10.1016/j.apsusc.2019.04.255>.
- [12] Rodrigues TA, Duarte V, Avila JA, Santos TG, Miranda RM, Oliveira JP. Wire and arc additive manufacturing of HSLA steel: effect of thermal cycles on microstructure and mechanical properties. *Addit Manuf* 2019;27:440–50. <https://doi.org/10.1016/j.addma.2019.03.029>.
- [13] Wu B, Ding D, Pan Z, Cuiuri D, Li H, Han J, et al. Effects of heat accumulation on the arc characteristics and metal transfer behavior in Wire Arc Additive Manufacturing of Ti6Al4V. *J Mater Process Technol* 2017;250:304–12. <https://doi.org/10.1016/j.jmatprotec.2017.07.037>.
- [14] Wu B, Pan Z, Ding D, Cuiuri D, Li H. Effects of heat accumulation on microstructure and mechanical properties of Ti6Al4V alloy deposited by wire arc additive manufacturing. *Addit Manuf* 2018;23:151–60. <https://doi.org/10.1016/j.addma.2018.08.004>.
- [15] Zhao H, Zhang G, Yin Z, Wu L. Effects of interpass idle time on thermal stresses in multipass multilayer weld-based rapid prototyping. *J Manuf Sci Eng* 2013;135:011016. <https://doi.org/10.1115/1.4023363>.
- [16] Montevecchi F, Venturini G, Grossi N, Scippa A, Campatelli G. Idle time selection for wire-arc additive manufacturing: a finite element-based technique. *Addit Manuf* 2018;21:479–86. <https://doi.org/10.1016/j.addma.2018.01.007>.
- [17] Lei Y, Xiong J, Li R. Effect of inter layer idle time on thermal behavior for multi-layer single-pass thin-walled parts in GMAW-based additive manufacturing. *Int J Adv Manuf Technol* 2018;96:1355–65. <https://doi.org/10.1007/s00170-018-1699-1>.
- [18] Wu B, Pan Z, Ding D, Cuiuri D, Li H, Fei Z. The effects of forced interpass cooling on the material properties of wire arc additively manufactured Ti6Al4V alloy. *J Mater Process Technol* 2018;258:97–105. <https://doi.org/10.1016/j.jmatprotec.2018.03.024>.
- [19] Wu B, Pan Z, Chen G, Ding D, Yuan L, Cuiuri D, et al. Mitigation of thermal distortion in wire arc additively manufactured Ti6Al4V part using active interpass cooling. *Sci Technol Weld Join* 2019;0:1–11. <https://doi.org/10.1080/13621718.2019.1580439>.
- [20] Montevecchi F, Venturini G, Grossi N, Scippa A, Campatelli G. Heat accumulation prevention in Wire-Arc-Additive-Manufacturing using air jet impingement. *Manuf Lett* 2018;17:14–8. <https://doi.org/10.1016/j.mfglet.2018.06.004>.
- [21] Hackenhaar W, Mazzaferro JAE, Montevecchi F, Campatelli G. An experimental-numerical study of active cooling in wire arc additive manufacturing. *J Manuf Process* 2020;52:58–65. <https://doi.org/10.1016/j.jmapro.2020.01.051>.

- [22] Nagamatsu H, Sasahara H, Mitsutake Y, Hamamoto T. Development of a cooperative system for wire and arc additive manufacturing and machining. *Addit Manuf* 2020;31:100896. <https://doi.org/10.1016/j.addma.2019.100896>.
- [23] da Silva LJ, Souza DM, de Araújo DB, Reis RP, Scotti A. Concept and validation of an active cooling technique to mitigate heat accumulation in WAAM. *Int J Adv Manuf Technol* 2020;107:2513–23. <https://doi.org/10.1007/s00170-020-05201-4>.
- [24] Reissen U, Sharma R, Mann S, Oster L. Increasing the manufacturing efficiency of WAAM by advanced cooling strategies. *Weld World* 2020. <https://doi.org/10.1007/s40194-020-00930-2>.
- [25] Derekar KS. A review of wire arc additive manufacturing and advances in wire arc additive manufacturing of aluminium. *Mater Sci Technol* 2018;34:895–916. <https://doi.org/10.1080/02670836.2018.1455012>.
- [26] Bajaj P, Hariharan A, Kini A, Kürsteiner P, Raabe D, Jäggle EA. Steels in additive manufacturing: a review of their microstructure and properties. *Mater Sci Eng A* 2020;772:138633. <https://doi.org/10.1016/j.msea.2019.138633>.
- [27] Jin W, Zhang C, Jin S, Tian Y, Wellmann D, Liu W. Wire arc additive manufacturing of stainless steels: a review. *Appl Sci (Basel)* 2020;10. <https://doi.org/10.3390/app10051563>.
- [28] Rafeezad M, Ghaffari M, Vahedi Nemani A, Nasiri A. Microstructural evolution and mechanical properties of a low-carbon low-alloy steel produced by wire arc additive manufacturing. *Int J Adv Manuf Technol* 2019;105:2121–34. <https://doi.org/10.1007/s00170-019-04393-8>.
- [29] Le VT. A preliminary study on gas metal arc welding-based additive manufacturing of metal parts. *Sci Technol Dev J* 2020;23:422–9. <https://doi.org/10.32508/stdj.v23i1.1714>.
- [30] Haden CV, Zeng G, Carter FM, Ruhl C, Krick BA, Harlow DG. Wire and arc additive manufactured steel: tensile and wear properties. *Addit Manuf* 2017;16:115–23. <https://doi.org/10.1016/j.addma.2017.05.010>.
- [31] Chen X, Li J, Cheng X, He B, Wang H, Huang Z. Microstructure and mechanical properties of the austenitic stainless steel 316L fabricated by gas metal arc additive manufacturing. *Mater Sci Eng A* 2017;703:567–77. <https://doi.org/10.1016/j.msea.2017.05.024>.
- [32] Yang Y, Gong Y, Qu S, Rong Y, Sun Y, Cai M. Densification, surface morphology, microstructure and mechanical properties of 316L fabricated by hybrid manufacturing. *Int J Adv Manuf Technol* 2018;1–10. <https://doi.org/10.1007/s00170-018-2144-1>.
- [33] Wu W, Xue J, Zhang Z, Yao P. Comparative study of 316L depositions by two welding current processes. *Mater Manuf Process* 2019;34:1502–8. <https://doi.org/10.1080/10426914.2019.1643473>.
- [34] Wu W, Xue J, Wang L, Zhang Z, Hu Y, Dong C. Forming process, microstructure, and mechanical properties of thin-walled 316L stainless steel using speed-cold-welding additive manufacturing. *Metals (Basel)* 2019;9. <https://doi.org/10.3390/met9010109>.
- [35] Abioye TE, Medrano-Tellez A, Farayibi PK, Oke PK. Laser metal deposition of multi-track walls of 308LSI stainless steel. *Mater Manuf Process* 2017;32:1660–6. <https://doi.org/10.1080/10426914.2017.1292034>.
- [36] Li M, Lu T, Dai J, Jia X, Gu X, Dai T. Microstructure and mechanical properties of 308L stainless steel fabricated by laminar plasma additive manufacturing. *Mater Sci Eng A* 2020;770:138523. <https://doi.org/10.1016/j.msea.2019.138523>.
- [37] Van Thao L, Dinh Si M, Tat Khoa D, Quang Huy H. Prediction of welding bead geometry for wire arc additive manufacturing of SS308L walls using response surface methodology. *Transp Commun Sci J* 2020;71:431–43. <https://doi.org/10.25073/tcsj.71.4.11>.
- [38] Le VT, Mai DS. Microstructural and mechanical characteristics of 308L stainless steel manufactured by gas metal arc welding-based additive manufacturing. *Mater Lett* 2020;271:127791. <https://doi.org/10.1016/j.matlet.2020.127791>.
- [39] Yang D, Wang G, Zhang G. Thermal analysis for single-pass multi-layer GMAW based additive manufacturing using infrared thermography. *J Mater Process Technol* 2017;244:215–24. <https://doi.org/10.1016/j.jmatprotec.2017.01.024>.
- [40] Herzog D, Seyda V, Wycisk E, Emmelmann C. Additive manufacturing of metals. *Acta Mater* 2016;117:371–92. <https://doi.org/10.1016/j.actamat.2016.07.019>.
- [41] Gong H, Rafi K, Gu H, Janaki Ram GD, Starr T, Stucker B. Influence of defects on mechanical properties of Ti–6Al–4V components produced by selective laser melting and electron beam melting. *Mater Des* 2015;86:545–54. <https://doi.org/10.1016/j.matdes.2015.07.147>.
- [42] Li SJ, Murr LE, Cheng XY, Zhang ZB, Hao YL, Yang R, et al. Compression fatigue behavior of Ti–6Al–4V mesh arrays fabricated by electron beam melting. *Acta Mater* 2012;60:793–802. <https://doi.org/10.1016/j.actamat.2011.10.051>.
- [43] Leuders S, Thöne M, Riemer A, Niendorf T, Tröster T, Richard HA, et al. On the mechanical behaviour of titanium alloy TiAl6V4 manufactured by selective laser melting: fatigue resistance and crack growth performance. *Int J Fatigue* 2013;48:300–7. <https://doi.org/10.1016/j.ijfatigue.2012.11.011>.
- [44] Fu JW, Yang YS, Guo JJ, Ma JC, Tong WH. Microstructure evolution in AISI 304 stainless steel during near rapid directional solidification. *Mater Sci Technol* 2009;25:1013–6. <https://doi.org/10.1179/174328408X317093>.
- [45] Li K, Li D, Liu D, Pei G, Sun L. Microstructure evolution and mechanical properties of multiple-layer laser cladding coating of 308L stainless steel. *Appl Surf Sci* 2015;340:143–50. <https://doi.org/10.1016/j.apsusc.2015.02.171>.
- [46] En Z, Tan E, Hock J, Pang L, Kaminski J, Pepin H. Characterisation of porosity, density, and microstructure of directed energy deposited stainless steel AISI 316L. *Addit Manuf* 2019;25:286–96. <https://doi.org/10.1016/j.addma.2018.11.014>.
- [47] Wang L, Xue J, Wang Q. Correlation between arc mode, microstructure, and mechanical properties during wire arc additive manufacturing of 316L stainless steel. *Mater Sci Eng A* 2019;751:183–90. <https://doi.org/10.1016/j.msea.2019.02.078>.
- [48] Yin H, Felicelli SD. Dendrite growth simulation during solidification in the LENS process. *Acta Mater* 2010;58:1455–65. <https://doi.org/10.1016/j.actamat.2009.10.053>.
- [49] Singh KK, Sangal S, Murty GS. Hall-Petch behaviour of 316L austenitic stainless steel at room temperature. *Mater Sci Technol* 2002;18:165–72. <https://doi.org/10.1179/026708301125000384>.
- [50] Zhang K, Wang S, Liu W, Shang X. Characterization of stainless steel parts by Laser Metal Deposition Shaping. *Mater Des* 2014;55:104–19. <https://doi.org/10.1016/j.matdes.2013.09.006>.